Research Square

Preprints are preliminary reports that have not undergone peer review.
They should not be considered conclusive, used to inform clinical practice,
or referenced by the media as validated information.

PIV Investigation of Phase-Dependent Inter-Wing Aerodynamic Interaction in Dragonfly-like Tandem Flapping Wings

Sifan Guo
Beihang University
Mengzong Zheng
Beihang University
Guanting Su
Beihang University
Jinze Liang
liangjinze@buaa.edu.cn
Beihang University
Qiushi Li
Beihang University

Research Article

Keywords: dragonfly, tandem flapping wings, phase difference, inter-wing aerodynamic interaction, particle image velocimetry, induced-flow effect

Posted Date: November 18th, 2026

DOI: https://doi.org/10.21203/rs.3.rs-11571919/v1

License: This work is licensed under a Creative Commons Attribution 4.0 International License.
Read Full License

Additional Declarations: No competing interests reported.

PIV Investigation of Phase-Dependent Inter-Wing Aerodynamic Interaction in Dragonfly-like Tandem Flapping Wings

Sifan Guo[a], Mengzong Zheng[b,c,e], Guanting Su[b,c,e], Jinze Liang[c,*], Qiushi Li[a,b,c,d]
[a] *School of Energy and Power Engineering, Beihang University, Beijing 100191, China*
[b] *National Key Laboratory of Science and Technology on Aero-Engine Aero-thermodynamics, Beihang University, Beijing 100191, China*
[c] *Research Institute of Aero-Engine, Beihang University, Beijing 100191, China*
[d] *Engineering Research Center of Intelligent Air-Ground Integration Vehicle and Control, Ministry of Education, Xihua University, Chengdu 610039, China*
[e] *Sichuan Tianqiong Zhichuang Innovation Technology Co., Ltd., Meishan 620564, China*
**Correspondence: liangjinze@buaa.edu.cn;*

ABSTRACT

The phase difference between the forewing and hindwing is an important parameter affecting the aerodynamic performance of dragonfly-like tandem flapping wings. Based on a dynamically scaled tandem-wing flapping experimental platform, this study combines six-axis force measurements with particle image velocimetry (PIV) to investigate the lift variations of the forewing, hindwing, and tandem wings under different phase differences. The inter-wing flow structures at typical phase differences are also analyzed. To mitigate laser-sheet blockage and flow-field distortion, aerodynamic force measurements are used to guide the selection of representative phase differences for subsequent PIV measurements. The experimental results show that the mean lift of the tandem wings is relatively high when the forewing and hindwing flap nearly in phase. When the phase difference is 180°, the mean lift of the tandem wings reaches its minimum value, and the hindwing is more strongly affected by the phase difference than the forewing. The PIV results show that in-phase flapping enhances the downward induced flow due to the same-direction motion of the forewing and hindwing, which is conducive to lift enhancement. In contrast, out-of-phase flapping weakens the downward induced flow because the forewing and hindwing move in opposite directions, leading to a reduction in lift. The combined force and PIV results support an induced-flow-mediated vortex-interaction mechanism, in which phase-dependent modifications of the local induced velocity field and neighboring vortex structures are associated with changes in aerodynamic force generation. The present experimental results can provide a basis for kinematic design and aerodynamic optimization of dragonfly-inspired flapping-wing vehicles.

Keywords: dragonfly; tandem flapping wings; phase difference; inter-wing aerodynamic interaction; particle image velocimetry; induced-flow effect

1. Introduction

Flapping-wing micro aerial vehicles (MAVs) have attracted considerable attention because of their potential applications in environmental monitoring, disaster response, and operations in confined environments (Floreano and Wood 2015; Salami et al. 2022; Song et al. 2023; Liang et al. 2025). At the low Reynolds numbers characteristic of insect flight, aerodynamic force generation is strongly influenced by unsteady flow phenomena. Previous studies have identified leading-edge vortex (LEV) formation, rotational circulation, wake capture, and wing–wake interaction as important mechanisms contributing to aerodynamic force generation (Ellington et al. 1996; Dickinson et al. 1999; Birch and Dickinson 2003; Lentink and Dickinson 2009). Subsequent investigations have further emphasized the importance of these unsteady mechanisms for understanding insect flight and developing bio-inspired flapping-wing systems (Chin and Lentink 2016; Bomphrey and Godoy-Diana 2018; Nabawy 2023). For insects with two pairs of wings, aerodynamic force generation becomes more complex because the flow structures produced by one wing pair may interact with the motion and wake of the other.

Biological observations have shown that dragonflies adopt different forewing–hindwing phase relationships under different flight conditions (Alexander 1984; Azuma and Watanabe 1988; Wakeling and Ellington 1997a; Rüppell and Hilfert-Rüppell 2020). Previous experimental and theoretical investigations have demonstrated that the phase relationship can affect aerodynamic force generation, wake interactions, and flight performance (Maybury and Lehmann 2004; Usherwood and Lehmann 2008; Takahashi et al. 2016; Zheng et al. 2016). Related studies have also examined the aerodynamic consequences of tandem-wing interactions under different kinematic and flight conditions (Li and Dong 2017; Nakata et al. 2020; Yang et al. 2025). These findings establish phase difference as an important parameter in tandem-wing aerodynamics. However, the influence of phase difference cannot be fully understood from the resulting aerodynamic forces alone, because changes in wing phasing also modify the induced velocity field and the interactions between the neighboring vortex structures. Extensive numerical investigations have examined the aerodynamic interactions between the forewing and hindwing. Early numerical investigations examined how forewing–hindwing interactions modify local inflow conditions, vortex behavior, and aerodynamic force generation (Lan and Mao 2001; Sun and Lan 2004; Wang and Sun 2005). Further numerical studies have shown that changes in phase difference, wing spacing, and wake interactions can affect the aerodynamic performance and power requirements of tandem flapping wings(Wang and Russell 2007; Broering et al. 2012; Broering and Lian 2012). Experimental investigations have provided complementary evidence of the aerodynamic effects associated with wing phasing and tandem-wing interaction(Maybury and Lehmann 2004; Zheng et al. 2016; Peng et al. 2021). Collectively, these studies have established that phase difference influences aerodynamic performance through complex wing–wing interactions. However, these conclusions mainly rely on computed flow fields. Although numerical simulations provide valuable insights into

unsteady flapping aerodynamics, their predictions depend on numerical resolution, modeling assumptions, and prescribed wing kinematics. This sensitivity is more evident during strongly unsteady processes such as leading-edge vortex shedding, wake capture, and wing–vortex interaction. In these processes, some small-scale vortices, shear-layer evolution, and local induced-flow details may be smoothed or weakened. Independent experimental flow-field measurements are particularly valuable for establishing a relationship between local flow structures and aerodynamic force generation. Such measurements can help relate instantaneous aerodynamic force variations to the corresponding flow structures. Therefore, experimental investigations combining aerodynamic force measurements with phase-resolved flow-field observations are important for understanding the mechanisms underlying phase-dependent aerodynamic interactions. These experimental observations can complement numerical findings and provide additional evidence for interpreting phase-dependent aerodynamic interactions. Particle image velocimetry (PIV) provides experimentally measured velocity fields from which local vorticity distributions can be derived, allowing unsteady flow structures and induced-flow characteristics to be examined (Adrian 1991; Westerweel 1997; Raffel et al. 2018). However, PIV measurements of tandem flapping wings present additional challenges compared with isolated-wing measurements. Because the relative positions and orientations of the forewing and hindwing vary with phase difference and flapping phase, the non-target wing may obstruct the laser sheet or camera view. Reflection and refraction from the wing surfaces may also introduce missing or distorted flow-field information. These optical limitations complicate the acquisition of reliable flow-field measurements around both wings at representative flapping phases. Consequently, an appropriate selection of measurement conditions and synchronization of the PIV system with the prescribed wing motion are important for investigating phase-dependent aerodynamic interactions.

To address these challenges, the present study combines aerodynamic force measurements with phase-resolved PIV using a dynamically scaled dragonfly-inspired tandem-wing experimental platform (Peng et al. 2021). The phase difference between the forewing and hindwing is systematically varied, and the aerodynamic forces of the forewing, hindwing, and tandem-wing system are measured under 12 phase-difference configurations. Based on the cycle-averaged force results, the in-phase ($\lambda = 0°$) and out-of-phase ($\lambda = 180°$) conditions are selected for further PIV measurements at representative flapping phases. The corresponding flow structures are compared with those of isolated-wing flapping to examine the effects of wing–wing interaction on local induced flow and vortex behavior. By combining phase-dependent force measurements, sectional PIV observations, and spanwise vortex reconstructions, the present study aims to clarify the relationship among wing phasing, induced-flow modification, vortex interactions, and aerodynamic force generation. In addition, the force-guided selection of representative PIV conditions provides a practical approach to reducing optical blockage difficulties during tandem-wing flow measurements.

2. Methods

2.1. Kinematic Definition and Phase Difference

The wing motion of a dragonfly can be described by three Euler angles in the body-fixed coordinate system O′X′Y′Z′, namely the stroke angle θ, rotation angle α, and deviation angle δ, together with the stroke-plane angle β. As shown in Fig. 1(a,b), the stroke plane is defined by the trajectory of the wing tip and the wing root O′. The stroke-plane angle β is defined as the angle between the stroke plane and the horizontal plane. The stroke angle θ is defined as the angle between the Z'-axis and the projection L' of the line L connecting the wing root and wing tip onto the stroke plane. The stroke angle is defined as positive when the wing is above the horizontal plane. The rotation angle α represents the angle between the wing surface and the stroke plane, while the deviation angle δ represents the angle between L and L'. The phase difference λ is a characteristic kinematic parameter of dragonflies and describes the interaction between the forewing and hindwing. It is defined as the flapping phase difference between the forewing and hindwing. The phase difference is taken as positive when the hindwing leads the forewing. Based on previous biological observations, Berman and Wang (2007) parameterized insect wing motion during hovering flight. They proposed analytical functions composed of hyperbolic tangent and sine functions, which can accurately describe the variations in stroke and rotation angles. Therefore, these functions are adopted in this study to describe the stroke and rotation angles of dragonfly wings.

The stroke angle $\theta(t)$ can be expressed as:

$$\theta(t) = \frac{\theta_m}{-\sin^{-1}(C_\theta)} \sin^{-1}\left(C_\theta \cos\left(2\pi f(t+\lambda_\theta)\right)\right) + \theta_0 \tag{1}$$

where θ_m denotes half of the stroke angle amplitude, C_θ is a constant parameter controlling the periodic variation of the stroke angle, λ_θ is the phase-shift parameter of the stroke angle, and θ_0 is the mean stroke angle.

The rotation angle $\alpha(t)$ can be expressed as:

$$\alpha(t) = \frac{\alpha_m}{\tanh(C_\alpha)} \tanh\left[C_\alpha \sin\left(2\pi f(t+\lambda_\alpha)\right)\right] + \alpha_0 \tag{2}$$

where αm denotes half of the rotation angle amplitude, Cα is a constant parameter controlling the periodic variation of the rotation angle, λα is the phase-shift parameter of the rotation angle, and α0 is the mean rotation angle. Accordingly, the mid-upstroke and mid-downstroke angles of attack are defined as $\alpha_u = \alpha_0 + \alpha_m$ and $\alpha_d = \alpha_0 - \alpha_m$, respectively. Since the deviation angle is small in magnitude and varies irregularly, its influence is neglected in this study. In this study, the forewing and hindwing follow the same flapping kinematics, and the detailed parameters are listed in Table 1. Fig. 2 illustrates the prescribed variations of the stroke angle θ and rotation angle α over one normalized flapping cycle. The stroke angle varies approximately between −30° and 30°, while the rotation angle ranges

from about 65° to 170°. The mid-downstroke and mid-upstroke correspond to the normalized times T = *ft* = 0.25 and T = *ft* = 0.75, respectively. The forewing and hindwing follow the same prescribed kinematic profiles, and their relative motion is determined by the phase difference λ.

Table 1 The value of kinematic parameters

θ_m	C_θ	θ_0	α_m	C_α	α_d	α_u	$\lambda_{\theta,f}$	$\lambda_{\theta,h}$	$\lambda_{\alpha,f}$	$\lambda_{\alpha,h}$
30°	0.8	0°	52.5°	2.5	65°	170°	-0.25	0.25	-0.5	0

To ensure the similarity between the flow fields generated by the experimental model and those of real dragonflies during flapping flight, three key dimensionless parameters are considered: the Reynolds number (*Re*) based on the mean wingtip velocity, the Strouhal number (*St*), and the reduced frequency (*k*). These parameters characterize the unsteady aerodynamic behavior of flapping wings. Since the model wings in this study operate in water, the experimental conditions must be carefully designed to achieve dynamic similarity between the model and real dragonfly wings. Therefore, the experimental parameters are selected to ensure consistency in these key dimensionless parameters. The definitions and physical significance of these parameters are introduced below. Here, the Reynolds number *Re* is a dimensionless parameter that characterizes the effect of fluid viscosity during the flow process. It can be expressed as the ratio of inertial force to viscous force. Given a reference length L_{ref} and a reference velocity U_{ref}, the Reynolds number is defined as:

$$Re = \frac{\rho U_{\text{ref}} L_{\text{ref}}}{\mu} \tag{3}$$

where ρ is the fluid density and μ is the dynamic viscosity of the fluid. In flapping flight, the wings generate vertical lift and horizontal thrust. Therefore, the mean chord length c_{m} is used as the reference length L_{ref}. During hovering flight, the mean flapping velocity of the wing tip is adopted in the present study as the reference velocity. It is defined as $U_{\text{ref}} = U_{\text{tip}} = \omega R$, where ω is the mean angular velocity of wing flapping $\omega = 2\phi f$, ϕ is the stroke amplitude in radians, and *R* is the wing span. For non-hovering flight, the Strouhal number *St* is introduced to characterize wake vortex dynamics and vortex shedding behavior:

$$St = \frac{f L_{\text{ref}}}{U_{\text{ref}}} \tag{4}$$

By comparing the spatial wavelength of the flow disturbance with the chord length, the reduced frequency *k* provides a dimensionless parameter for characterizing the unsteadiness of flapping flight. The reduced frequency is defined by the flapping angular velocity ω, the mean chord length *c*, and the reference velocity U_{ref}:

$$k = \frac{\pi f c}{U_{\text{ref}}} \tag{5}$$

The model wing profiles were extracted from the forewing and hindwing of Pantala flavescens and enlarged by a factor of five. The model wings were fabricated from transparent optical quartz glass and were treated as rigid wings throughout the experiments. Therefore, the aerodynamic effects of wing flexibility were not considered in the present study. The flapping frequency is set to 0.1 Hz. The model forewing has a span of 17.4 cm, a mean chord length of 3.5 cm, and a surface area of 60.9 cm². The model hindwing has a span of 16.9 cm, a mean chord length of 4.6 cm, and a surface area of 77.7 cm². As shown in Fig. 3, the forewing has a relatively slender planform, whereas the hindwing exhibits a broader chordwise profile, particularly near the wing root. At a flapping frequency of 0.1 Hz, the flapping Reynolds numbers of the model forewing and hindwing are 1642 and 2109, respectively. The corresponding Strouhal numbers are 0.12 and 0.13, and the reduced frequencies are 0.40 and 0.36, respectively. These values are consistent with the range observed in real dragonfly hovering flight (Re = 1000–2000, St = 0.11–0.15, and k = 0.25–0.40 (Wakeling and Ellington 1997b)). Therefore, the model experiment achieves dimensionless parameter similarity with real dragonfly flapping flight and can reproduce the main flow-field characteristics of dragonfly wing motion.

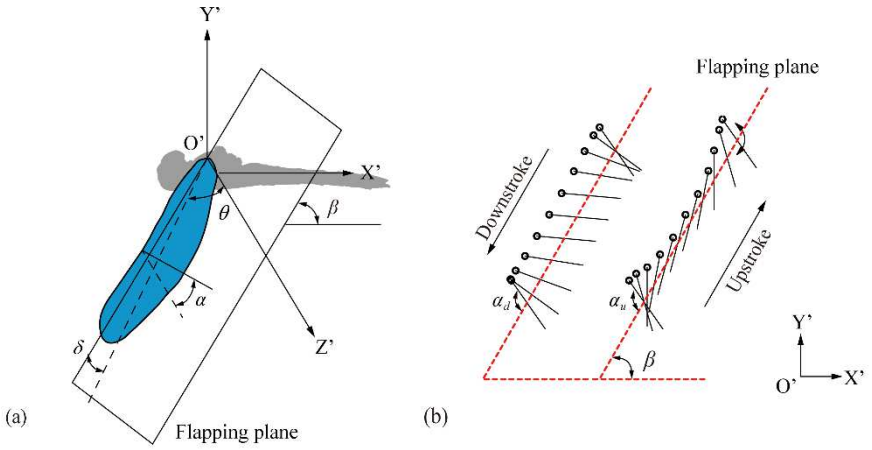


Fig. 1. Definition of kinematic parameters of the dragonfly wing (Zheng et al. 2026) (a) Flapping plane and flapping plane angle ; (b) Wing cross-sectional orientation.

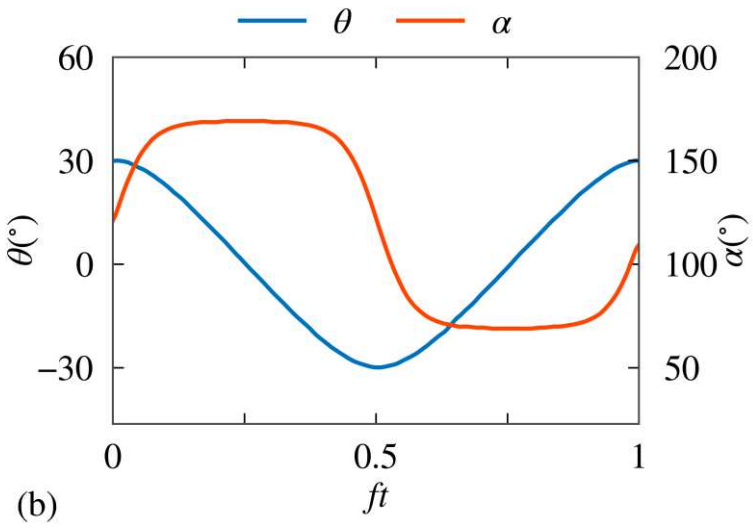


Fig. 2. Time histories of the prescribed stroke angle θ and rotation angle α over one normalized flapping cycle.

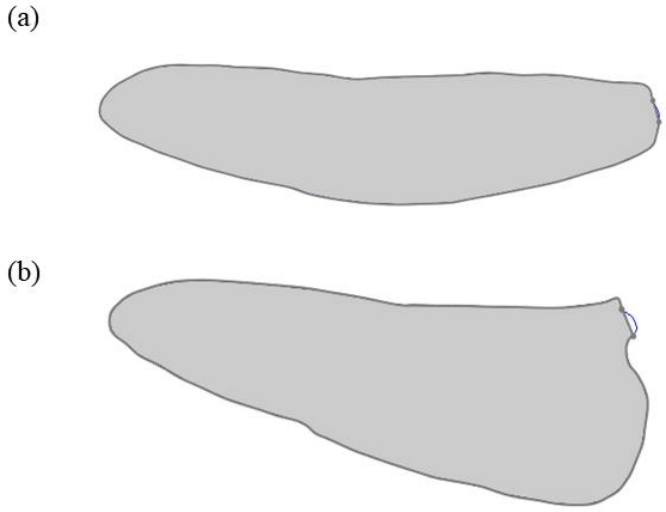


Fig. 3. Planform geometries of the dragonfly-inspired model wings: (a) forewing; (b) hindwing.

2.2. Tandem-Wing Model Experimental System

The experimental system consists of a 1 m × 1 m × 1 m glass water tank, a mechanical control system, a force measurement system, and a PIV measurement system (Zheng et al. 2024), as shown in Fig. 4. The water depth is 900 mm. The wing models were positioned inside the tank to reduce possible interference from the surrounding boundaries. The system can reproduce the flapping and rotational motions of dragonfly forewings and hindwings. It can also obtain the aerodynamic

forces and flow-field information of the model wings at specified times and spatial locations. Different from single-wing flapping experiments, this study focuses on the aerodynamic interaction between the forewing and hindwing with a phase difference. Therefore, the experimental platform is not only used to reproduce the motion of a single wing. It is designed to ensure that the forewing and hindwing flap in tandem with a prescribed phase relationship. During this process, the forces on the forewing and hindwing, as well as the flow fields at typical sections, are measured.

Unlike a single-wing platform, this system arranges two independent wing-driving systems along the X-axis to simulate the forewing and hindwing motions, as shown in Fig. 5. Each driving system is equipped with a self-designed parallel differential gearbox. Two high-resolution servo motors are used to jointly control the flapping and rotation degrees of freedom of each wing. Compared with the serial scheme in which each degree of freedom is driven by an independent motor, the parallel differential scheme reduces the mechanism size while maintaining transmission accuracy. This miniaturization provides an important advantage for tandem-wing studies. It allows the axial spacing ratio between the model forewing and hindwing to match that of real dragonflies. The spacing is set to 0.8–1.0 times the mean chord length based on biological measurements. Thus, the inter-wing geometric relationship can be reproduced more realistically. In the experiments, the single-wing kinematics of the forewing and hindwing remain unchanged (Zheng et al. 2024). Only the phase difference between the two wings is varied. This ensures that the differences between different cases mainly result from changes in the relative phase between the forewing and hindwing. A six-axis force/torque sensor is installed at the root of each wing. The sensors have a measurement range of ±25 N in the X and Y directions and 35 N in the Z direction, with a resolution of 1/160 N. Therefore, the variations in the aerodynamic forces of the forewing, hindwing, and tandem wings with phase difference can be further obtained. The lift coefficient C_L is calculated as:

$$C_L = \frac{L}{0.5\rho S U_{\text{ref}}^2} \tag{6}$$

where S is the surface area of the model wing, and U_{ref} is the mean flapping velocity of the wing tip.

The repeatability and uncertainty of the force and PIV measurements were further evaluated following the procedures used in our previous experimental studies (Zheng et al. 2024, 2026). For each force-measurement case, 20 complete flapping cycles were recorded. To avoid the influence of start-up and stopping processes, the data from the 4th to the 18th cycles were used for phase-averaged force analysis. The force signals were processed using a zero-phase-lag low-pass Butterworth filter with a cut-off frequency of 2 Hz. The uncertainty of the aerodynamic coefficients was estimated by considering the measurement errors of the three force components, the deviations of the stroke and rotation angles, the fluid-density variation caused by temperature fluctuation, and the flapping-frequency error. The relative errors of the force signals in the X′, Y′, and Z′ directions were 0.45%, 0.47%, and 0.75%, respectively. The deviations of the stroke and rotation angles were 0.75% and 0.67%,

respectively. The density error was 0.049%, and the flapping-frequency error was 0.2%. Based on uncertainty propagation, the total uncertainty of the aerodynamic coefficients was approximately 1.43%. For the PIV measurements, a high-speed CCD camera with a resolution of 2456 × 2056 pixels and a Nikon 24 mm/F2.8 lens was used with a double-pulse laser system. The laser wavelength was 532 nm, the pulse energy was 200 mJ, and the laser sheet thickness was adjusted to approximately 1 mm. Hollow glass beads with a diameter of 10 μm, a density of 1.05×10^3 kg/m³, and a refractive index of 1.33 were used as tracer particles. At each measurement position and phase, 20 image pairs were acquired, and the 4th to 18th image pairs were averaged to obtain the velocity and vorticity fields. The image pairs were processed using Micro Vec V3 software with a 64 × 64 pixel interrogation window. Sub-pixel Gaussian fitting, median filtering, and an iterative algorithm were used to improve the accuracy of the vector fields and remove spurious vectors.

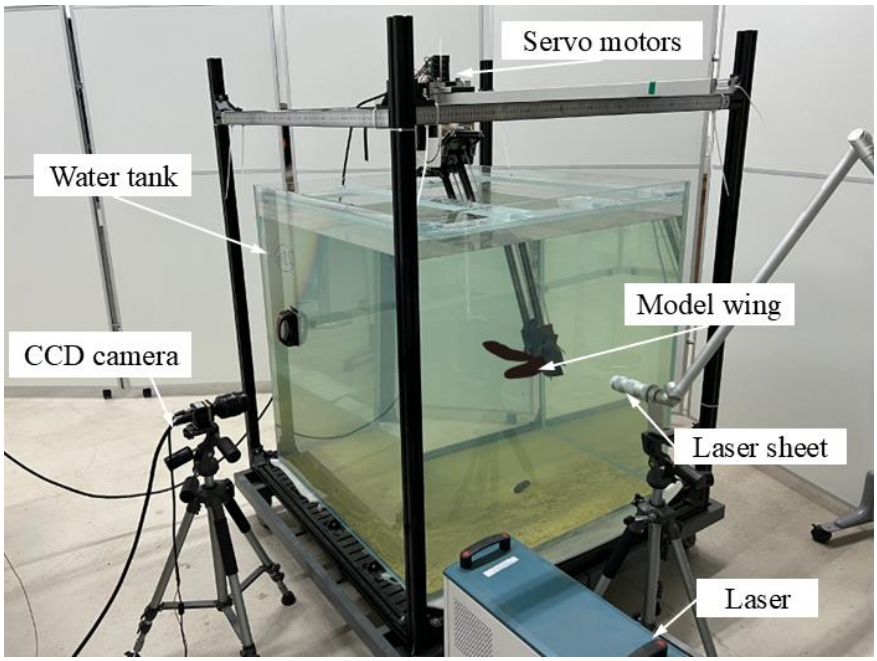


Fig. 4. Photograph of the experimental setup (Zheng et al. 2024)

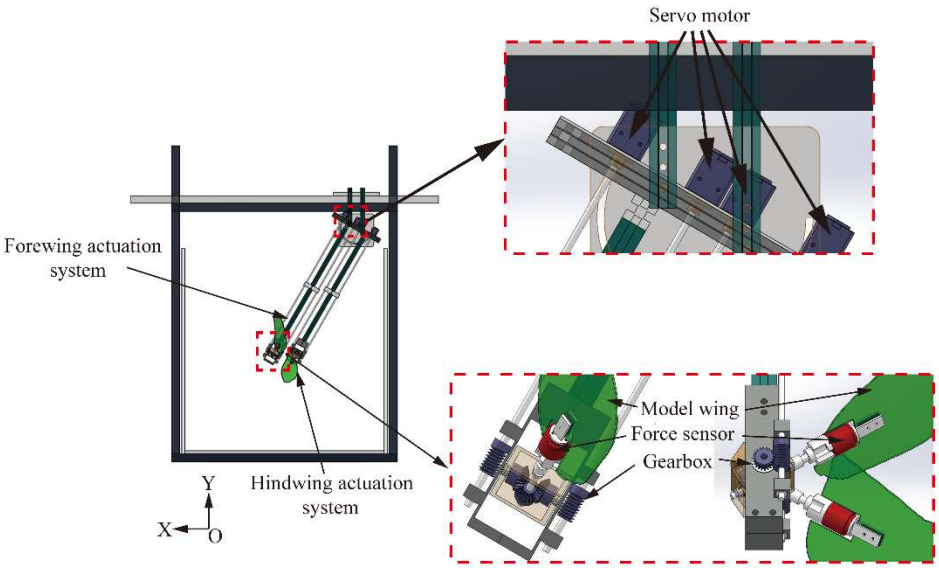


Fig. 5. Schematic diagram of the flapping mechanism (Zheng et al. 2026)

2.3 PIV Measurement Setup and Laser-Blockage Treatment for Tandem Wings

Based on the phase-difference distribution of dragonflies under different flight states, a parametric study is conducted with an interval of 30°. Twelve phase differences, ranging from 0° to 330° in increments of 30°, were investigated. The selected phase differences are 0°, 30°, 60°, 90°, 120°, 150°, 180°, 210°, 240°, 270°, 300°, and 330°. According to the definition of phase difference, the flapping kinematics at 0° and 360° are identical. Therefore, the case of 360° is not repeated in the experiment. During PIV measurements, the forewing and hindwing are located at different flapping positions because of the phase difference. According to the working principle of PIV, when the model wing surface is not perpendicular to the laser sheet, the wing between the laser sheet and the camera can block the flow field. Meanwhile, scattering and refraction occur on the wing surface, resulting in missing and distorted flow-field information. As shown in Fig. 6, the forewing surface is perpendicular to the laser sheet and does not block the laser. It is therefore located at an ideal position for PIV measurement. In this case, the tracer particles near the wing are illuminated by the laser, and complete flow-field information around the wing can be obtained. However, the hindwing surface forms an angle with the laser sheet. As the laser passes through the hindwing surface, blockage and refraction occur. As a result, tracer particles in some regions cannot be illuminated, or particles outside the measurement plane are illuminated, leading to flow-field distortion.

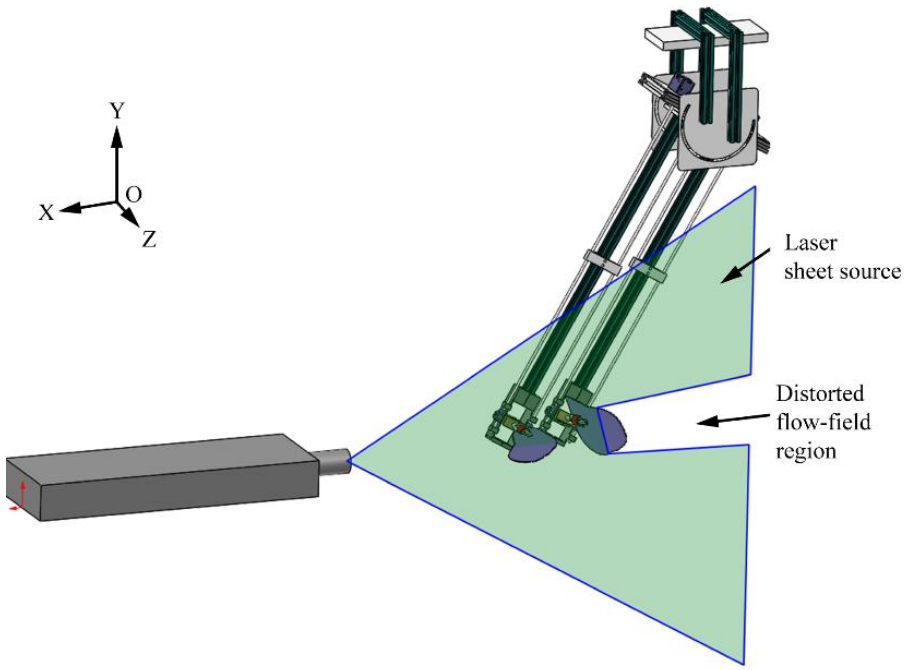


Fig. 6. Flow-field distortion induced by wing blockage of the laser sheet

To address the above flow-field measurement problems, the imaging instant should first be determined. The positions of the laser sheet and camera are then adjusted according to the relative positions of the forewing and hindwing at this instant. This adjustment is used to minimize the disturbance caused by the wing positions during flow-field measurement. However, each adjustment of the laser sheet and camera requires refocusing and recalibration of the PIV system, which is highly time-consuming. Therefore, the PIV measurement strategy for tandem flapping wings in this study is based on force-guided case selection. The aerodynamic forces of the tandem wings are first analyzed, and the relationship between force generation and phase difference is then obtained. Based on this relationship, in-phase flapping (λ=0°) and out-of-phase flapping (λ=180°) are selected as representative cases for subsequent PIV measurements. After the characteristic phase differences are determined, the PIV setup is further adjusted according to the target wing and the target imaging instant. Instead of using a fixed configuration to measure the entire tandem-wing flow field at once, phase-resolved alignment is conducted based on the target wing. The laser sheet is placed at the r_2 chordwise section of the target wing, and the camera optical axis is kept perpendicular to the laser sheet. This ensures that the near-wing region of the target wing is measured under relatively ideal conditions. For different target instants and spanwise sections, the periodic repeatability of the flapping motion is used. Under LabVIEW phase-locked triggering, the same flapping motion is repeated, and flow-field information in regions with no blockage or weak blockage is collected separately. By averaging, stitching, or comparing the local flow fields obtained at the same phase, relatively reliable near-wing flow-field results can be obtained for the characteristic phase differences. In essence, this method uses force measurements that are not affected by optical blockage to guide PIV measurements that are sensitive to blockage. Thus, it reduces the experimental adjustment cost and improves the

reliability of flow-field measurements at characteristic phase differences. The detailed PIV experimental procedure is shown in Fig. 7.

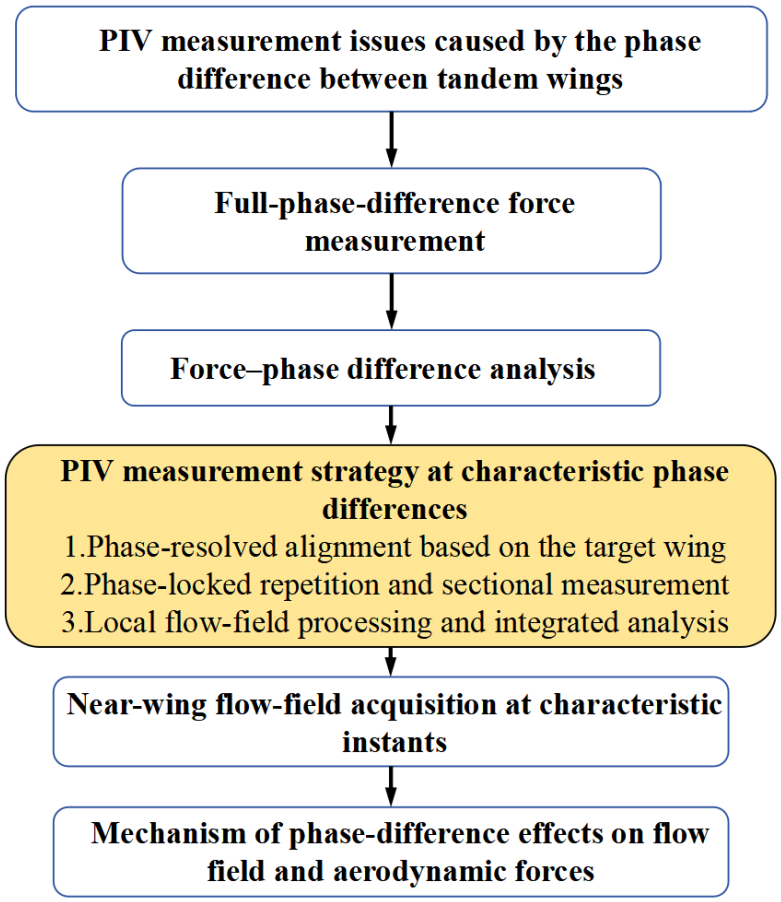


Fig. 7. Flowchart of the PIV Experiment for Tandem-Wing Phase Difference

3. Results

3.1 Effect of Phase Difference on Cycle-Averaged Aerodynamic Forces

Fig. 8 shows the variations in the cycle-averaged lift coefficients of the forewing $C_{L,f}$, hindwing $C_{L,h}$, and tandem wings $C_{L,t}$ with phase difference. It can be seen that the forewing lift coefficient $C_{L,f}$ reaches a maximum value of 1.60 at λ = 30°. As the phase difference increases, it gradually decreases and reaches a minimum value of 1.41 at λ = 180°. In the range of λ = 180°–300°, the forewing lift coefficient $C_{L,f}$ remains at a relatively low level, ranging from 1.41 to 1.43. When λ exceeds 300°, it increases significantly with increasing phase difference. Except for λ = 0°-60°, the forewing lift coefficient $C_{L,f}$ in tandem flapping is lower than that of the isolated forewing $C_{L,sf}$, which is 1.51. The maximum value of $C_{L,f}$ at λ = 30° is 13.48% higher than the minimum value at λ = 180°. It is also 5.96% higher than the lift coefficient of the isolated forewing $C_{L,sf}$.

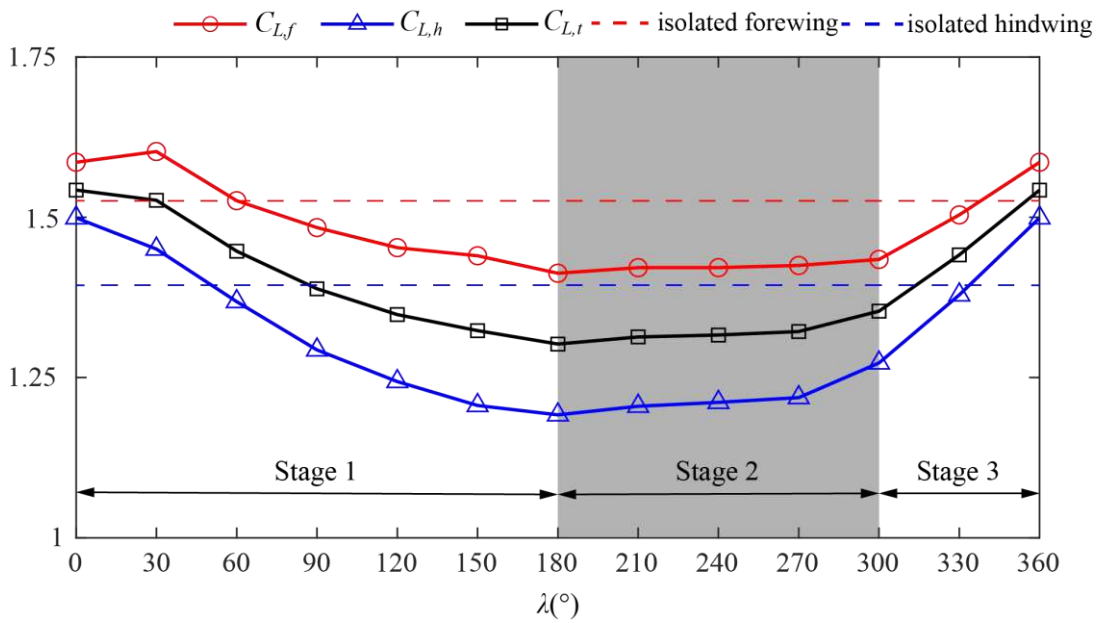


Fig. 8. Variation of the Mean Lift Coefficient with Phase Difference. (The values at 360° are periodic repetitions of the 0° values and do not represent additional experimental measurements.)

The hindwing lift coefficient $C_{L,h}$ reaches a maximum value of 1.50 at λ = 0°. As the phase difference increases, it gradually decreases and reaches a minimum value of 1.19 at λ = 180°. In the range of λ = 180°-300°, the hindwing lift coefficient $C_{L,h}$ remains at a relatively low level, ranging from 1.19 to 1.22. When λ exceeds 300°, it increases significantly with increasing phase difference. Except for λ = 0°–30°, the hindwing lift coefficient $C_{L,h}$ in tandem flapping is lower than that of the isolated hindwing $C_{L,sh}$, which is 1.39. The maximum value of $C_{L,h}$ at λ = 0° is 26.05% higher than the minimum value at λ = 180°. It is also 7.91% higher than the lift coefficient of the isolated hindwing $C_{L,sh}$. It can be seen that the forewing lift coefficient $C_{L,f}$ is generally larger than the hindwing lift coefficient $C_{L,h}$. This is because the hindwing has a larger surface area and a smaller span than the forewing, as indicated by Eq. (6). These geometric differences affect the normalization of the lift coefficient. However, the variations of the forewing and hindwing lift coefficients with phase difference are generally similar and can be divided into three stages. In the first stage, from λ = 0° to 180°, the lift coefficient decreases as the phase difference increases and reaches a minimum at λ = 180°. In the second stage, from λ = 180° to 300°, the lift coefficient remains at a relatively low level. In the third stage, from λ = 300° to 360°, the lift coefficient increases clearly with increasing phase difference.

The maximum values of the CL,f and CL,h occur at small phase differences, while their minimum values appear at λ = 180°. Except for small phase differences, namely λ = 0°–60° for the forewing and λ = 0°–30° for the hindwing, inter-wing aerodynamic interaction has a negative effect on lift generation. In other words, the lift coefficient of each wing in tandem flapping is lower than that of the corresponding isolated wing. The relative variation in the cycle-averaged hindwing lift coefficient across the tested phase differences is 26.05%, which is larger than the corresponding

variation of 13.48% for the forewing. This indicates that the cycle-averaged lift of the hindwing is more sensitive to changes in the forewing–hindwing phase difference.

The tandem-wing mean lift coefficient $C_{L,t}$ is jointly affected by $C_{L,f}$ and $C_{L,h}$. Therefore, these three lift coefficients show a similar variation trend with phase difference. The $C_{L,t}$ reaches a maximum value of 1.54 at λ = 0°. $C_{L,t}$ gradually decreases with increasing phase difference and reaches a minimum value of 1.30 at λ = 180°. In the range of λ = 180°–300°, $C_{L,t}$ remains at a relatively low level, ranging from 1.30 to 1.32. When λ exceeds 270°, $C_{L,t}$ increases clearly with increasing phase difference. The maximum value of $C_{L,t}$ at λ = 0° is 18.46% higher than the minimum value at λ = 180°.

3.2 Inter-Wing Aerodynamic Interaction at Characteristic Phase Differences

3.2.1 Aerodynamic Force Analysis under In-Phase and Out-of-Phase Flapping

As shown in Section 3.1, characteristic phase differences exist for the forewing and hindwing in tandem flapping. These phase differences correspond to the maximum and minimum lift values, namely λ = 0° and λ = 180°, respectively. Although the highest measured forewing lift coefficient occurs at λ = 30°, λ = 0° is selected as the representative high-lift condition because the total cycle-averaged lift coefficient of the tandem-wing system reaches its maximum at this phase difference. When λ = 0°, the forewing and hindwing follow the same motion pattern, which is defined as in-phase flapping. When λ = 180°, the forewing and hindwing move in opposite directions, which is defined as out-of-phase flapping.

Fig. 9(a) compares the instantaneous lift coefficient of the forewing in tandem flapping with that of the isolated forewing at λ = 0° and λ = 180°. Here, T = 0 denotes the beginning of the downstroke of the forewing. The results show that the effect of inter-wing aerodynamic interaction on forewing lift mainly appears near the mid-downstroke, at T = 0.25, as indicated by black box 1. During this period, the lift coefficient is the highest under in-phase flapping and the lowest under out-of-phase flapping. The lift coefficient of the isolated forewing lies between these two cases.

Fig. 9(b) compares the instantaneous lift coefficient of the hindwing in tandem flapping with that of the isolated hindwing at λ = 0° and λ = 180°. Here, T = 0 denotes the beginning of the downstroke of the hindwing. The results show that the effect of inter-wing aerodynamic interaction on hindwing lift mainly occurs near the mid-downstroke and mid-upstroke, at T = 0.25 and T = 0.75, respectively. Near the mid-downstroke, the lift coefficient is the highest under in-phase flapping and the lowest under out-of-phase flapping. The lift coefficient of the isolated hindwing lies between these two cases, as shown in black box 2. Near the mid-upstroke, the lift curve at λ = 0° is almost the same as that of the isolated hindwing. However, the lift curve at λ = 180° first decreases and then increases, as shown in black box 3. It should be noted that the aerodynamic influence of wing–wing interaction varies throughout the flapping cycle. Although in-phase flapping produces a higher cycle-averaged hindwing lift coefficient than isolated-wing flapping, the instantaneous lift enhancement is not maintained at every phase. As shown in Fig. 9(b), the hindwing

lift under in-phase flapping approaches or falls below the isolated-wing value during part of the downstroke.

Fig. 9(c) compares the total instantaneous lift coefficient of the tandem wings with that of the isolated wings at λ = 0° and λ = 180°. It can be seen that the lift curve of the tandem wings at λ = 0° is generally similar to that of the isolated wings. The wings are in the downstroke phase during T = 0–0.5, which is the main stage of lift generation. Near the mid-downstroke, at T = 0.25, the lift coefficient under in-phase flapping is higher than that of the isolated wings. This indicates that the inter-wing aerodynamic interaction is beneficial to lift enhancement at this instant. When λ = 180°, the forewing and hindwing flap out of phase and move in opposite directions. During T = 0–0.5, the forewing is in the downstroke phase, and the forewing mainly provides the lift. During T = 0.5–1, the hindwing is in the downstroke phase, and the hindwing mainly provides the lift.

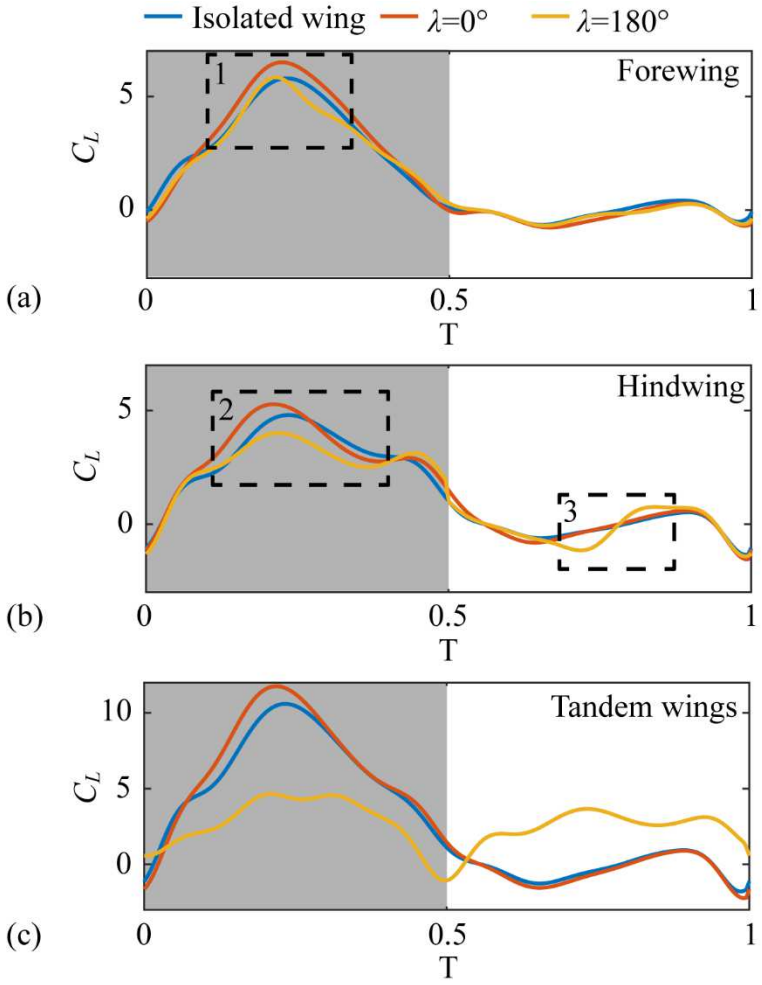


Fig. 9. Instantaneous Lift Coefficient Comparison between Tandem-Wing and Isolated-Wing Flapping at Characteristic Phase Differences

By analyzing the differences in the lift curves at characteristic phase differences, the characteristic instants at which inter-wing aerodynamic interaction affects lift are identified as T = 0.25 and T = 0.75. Therefore, the flow fields of the tandem wings at these instants need to be measured and analyzed. This analysis is used to reveal the

physical mechanism by which inter-wing aerodynamic interaction influences lift generation.

3.2.2 Flow-Field Characteristics under In-Phase and Out-of-Phase Flapping

Fig. 10(a) shows the vorticity and velocity fields at the r2 section of the tandem wings at λ = 0° and T = 0.25. For this experiment, the model wing mimicking the dragonfly forewing was selected, with r_2 = 0.61R. Meanwhile, ω* denotes the dimensionless vorticity, defined as ω* = ωc / *U*ref. Fig. 10(b,c) shows the flow fields of the isolated forewing and isolated hindwing at the same instant and section, respectively. By comparing the tandem-wing and isolated-wing flow fields, it can be seen that the inter-wing aerodynamic interaction mainly affects the flow near the forewing trailing-edge vortex and the hindwing leading-edge vortex during the mid-downstroke of in-phase flapping. During the downstroke of an isolated wing, the leading-edge vortex and trailing-edge vortex induce local rotational flow around the wing, as shown by the black boxes in Fig. 10(b,c). However, when the two wings flap in phase, the forewing and hindwing are close to each other and move downward synchronously. This weakens the structural stability of the forewing trailing-edge vortex and the hindwing leading-edge vortex, as shown by the black box in Fig. 10(a). The interaction between the neighboring vortices modifies their local structures and redistributes the induced velocity field between the two wings. The resulting flow pattern is consistent with an enhancement of the local downward induced flow near the mid-downstroke, which may contribute to the measured instantaneous lift enhancement.

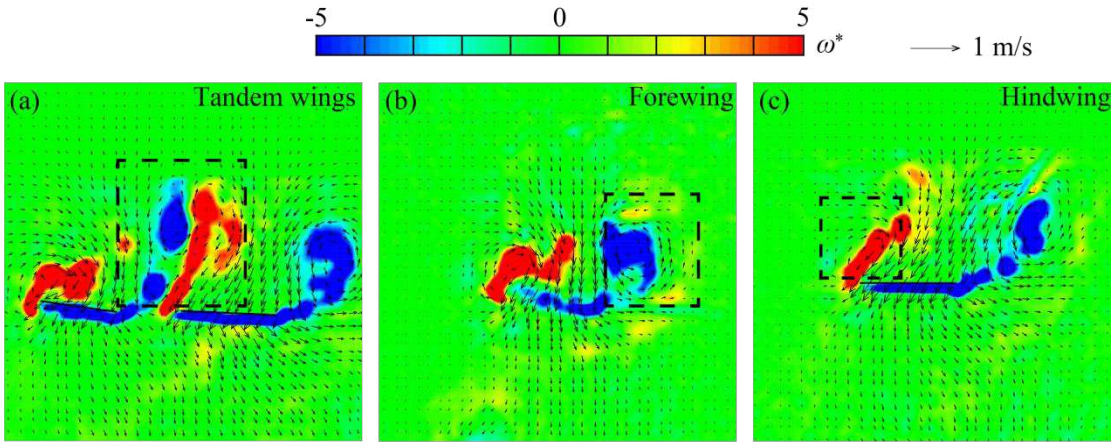


Fig. 10. Flow-Field Effect of Inter-Wing Aerodynamic Interaction at λ = 0° and Mid-Downstroke

Fig. 11(a) shows the vorticity and velocity fields at the r_2 section of the tandem wings at λ = 0° and T = 0.75. Fig. 11(b,c) shows the flow fields of the isolated forewing and isolated hindwing at the same instant and section, respectively. During the mid-upstroke under in-phase flapping, the forewing and hindwing move upward simultaneously. Owing to the asymmetry of the inclined stroke-plane kinematics, the leading-edge vortex and trailing-edge vortex are weak during the upstroke. As a result, the induced flow generated by these vortices is also weak. Therefore, when both wings are in the upstroke phase at the same time, the induced-flow effect has only a

small influence on lift. This also explains why, in Fig. 9, the inter-wing aerodynamic interaction has almost no effect on the lift of the forewing and hindwing during the upstroke under in-phase flapping.

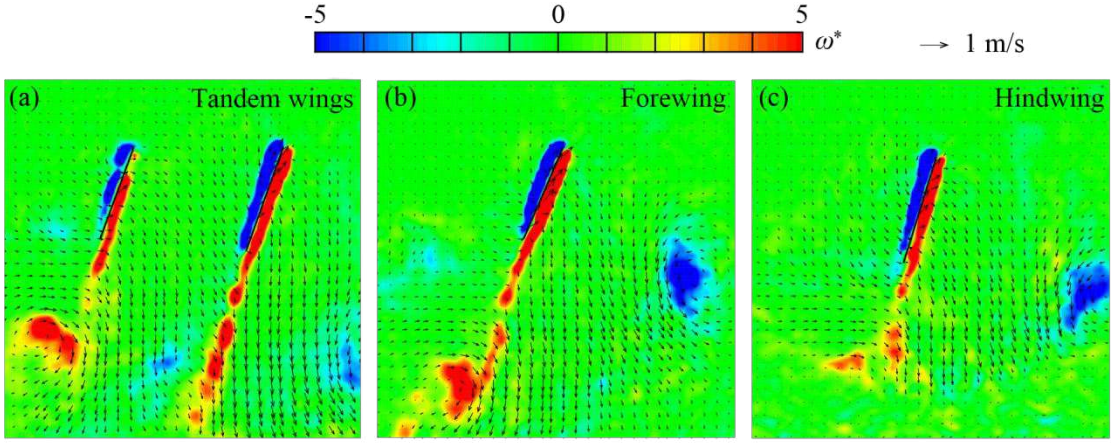


Fig. 11. Flow-Field Effect of Inter-Wing Aerodynamic Interaction at λ = 0° and Mid-Upstroke

Fig. 12(a) shows the vorticity and velocity fields at the r_2 section of the tandem wings at λ = 180° and T = 0.25. Fig. 12(b,c) shows the flow fields of the isolated forewing and isolated hindwing at the same instant and section, respectively. Under out-of-phase flapping, the forewing and hindwing move in opposite directions. At T = 0.25, the forewing is at the mid-downstroke, while the hindwing is at the mid-upstroke. At this instant, the upward motion of the hindwing interacts with the downward induced flow generated by the forewing, resulting in a local reduction in the downward velocity, as shown by the black box in Fig. 12(a). This interaction also modifies the flow field near the hindwing leading edge. Compared with isolated-wing flapping, the leading-edge vortex of the hindwing is displaced away from the wing surface and toward the forewing trailing-edge vortex. These two observations are closely related: the induced velocity field associated with the forewing trailing-edge vortex modifies the local flow around the hindwing, providing a possible explanation for the observed displacement of the hindwing LEV. In other words, the changes in downward induced flow and LEV position represent coupled responses to the aerodynamic interaction between the two wings. This interpretation is further supported by the spanwise vortex distribution in Fig. 16, where a similar displacement of the hindwing LEV can be observed. The modified flow field near the forewing is consistent with the reduction in forewing lift near the mid-downstroke in Fig. 9(a), while the altered hindwing LEV is associated with the hindwing force response during its upstroke, as shown in Fig. 9(b).

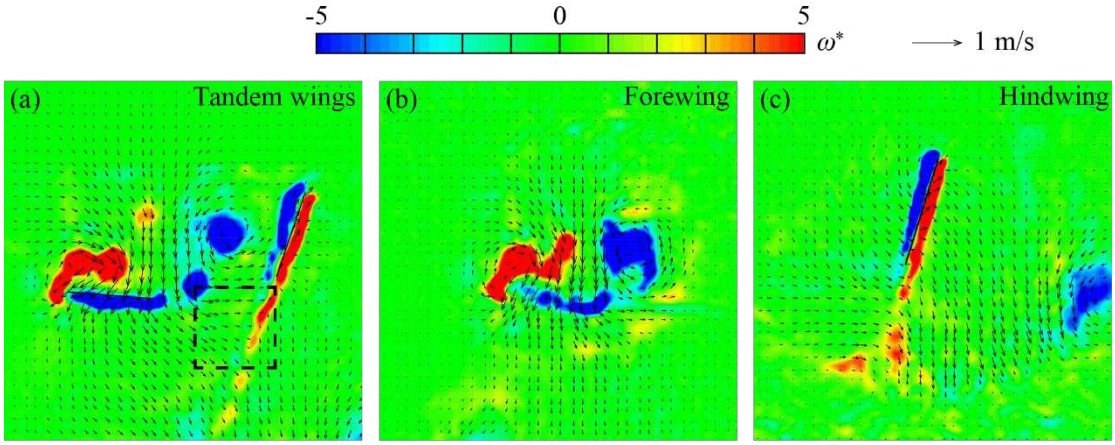


Fig. 12. Flow-field characteristics at λ = 180° and T = 0.25 (forewing mid-downstroke and hindwing mid-upstroke).

Fig. 13(a) shows the vorticity and velocity fields at the r2 section of the tandem wings at λ = 180° and T = 0.75. Fig. 13(b,c) shows the flow fields of the isolated forewing and isolated hindwing at the same instant and section, respectively. At this instant, the forewing is at the mid-upstroke, while the hindwing is at the mid-downstroke. The downwash generated by the hindwing during the downstroke is affected by the upward motion of the forewing. As a result, the downward velocity in some regions is weakened, as shown by the black box in Fig. 13(a). This modification of the induced flow is accompanied by changes in the vortex structures around the hindwing. As further illustrated by the spanwise-reconstructed vorticity distributions in Fig. 17, the apparent size of the hindwing leading-edge vortex is reduced compared with the isolated-wing condition. These observations suggest that the upward motion of the forewing modifies the local flow experienced by the hindwing during its downstroke, affecting the spatial organization of the hindwing LEV. The combined changes in the induced flow and LEV structure are consistent with the reduced hindwing lift observed near the mid-downstroke in Fig. 9(b).

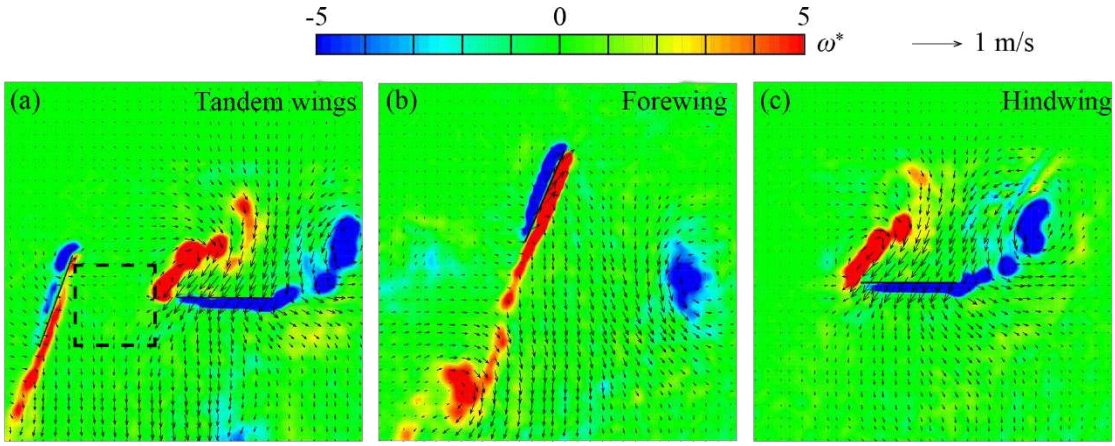


Fig. 13. Flow-field characteristics at λ = 180° and T = 0.75 (forewing mid-upstroke and hindwing mid-downstroke).

3.2.3 Spanwise Vortex Development under Inter-Wing Aerodynamic Interaction

Section 3.2.2 analyzed the PIV flow fields at the r_2 section for isolated-wing flapping, in-phase tandem flapping, and out-of-phase tandem flapping. Based on these results, the induced-flow effect was identified. This effect explains the aerodynamic characteristics of inter-wing aerodynamic interaction in tandem flapping wings.

The PIV system used in this experiment provides two-dimensional flow-field information. Although the two-dimensional flow field at a given section can reflect the main flow characteristics, flapping-wing motion is essentially three-dimensional. Since the wing rotates around the wing root, the spanwise sections closer to the wing tip have higher velocities. Under the influence of centrifugal force, vortex structures generated near the wing root can develop toward the wing tip. This spanwise flow is also an important factor in maintaining the stability of the leading-edge vortex. Therefore, flapping-wing motion has strong three-dimensional unsteady characteristics, and it is necessary to investigate the three-dimensional flow structures during flapping.

Because the geometries near the wing root and wing tip are complex, the flow fields in these regions are relatively disordered. These regions are also not the main contributors to aerodynamic force generation. Therefore, when measuring the spanwise development of vortex structures, the flow fields from 0.1R to 0.9R are measured at each experimental point, where R is the wing span. With an interval of 0.1R, each three-dimensional structure is reconstructed from nine two-dimensional sections uniformly distributed along the spanwise direction. To obtain the two-dimensional flow fields at different spanwise positions, the PIV system is kept fixed after each measurement. The laser sheet is then moved to a new measurement position by accurately adjusting the mechanical structure. The same flapping motion is repeated for each position. Thus, each experimental point requires nine repeated measurements. The nine two-dimensional flow fields are then stitched and integrated to obtain a three-dimensional flow-field slice at a given instant. Using this method, the three-dimensional flow-field distributions shown in Fig. 14–Fig. 17 are obtained.

Fig. 14(a) shows the three-dimensional flow field of in-phase tandem flapping when the forewing is at the mid-downstroke. Fig. 14(b,c) shows the three-dimensional flow fields of the isolated forewing and isolated hindwing at the same instant, respectively. It can be seen that the inter-wing aerodynamic interaction has a clear influence on the three-dimensional flow field. Under the induced-flow effect, the structures of the forewing trailing-edge vortex and the hindwing leading-edge vortex are significantly different from those of the isolated wings. The forewing and hindwing are close to each other and move downward synchronously. This weakens the structural stability of the forewing trailing-edge vortex and the hindwing leading-edge vortex. This flow characteristic is consistent with the two-dimensional analysis of the mid-downstroke flow field under in-phase flapping in Section 3.2.2.

Fig. 15(a) shows the three-dimensional flow field of in-phase tandem flapping when the forewing is at the mid-upstroke. Fig. 15(b,c) shows the three-dimensional flow fields of the isolated forewing and isolated hindwing at the same instant, respectively. At this instant, the forewing and hindwing are relatively far apart during the upstroke. The vortex structures generated by the two wings are also weak.

Therefore, the inter-wing aerodynamic interaction during the in-phase upstroke can be neglected. Compared with isolated-wing flapping, the flow fields generated by the forewing and hindwing under in-phase flapping show almost no obvious change. This flow characteristic is consistent with the two-dimensional analysis of the mid-upstroke flow field under in-phase flapping in Section 3.2.2.

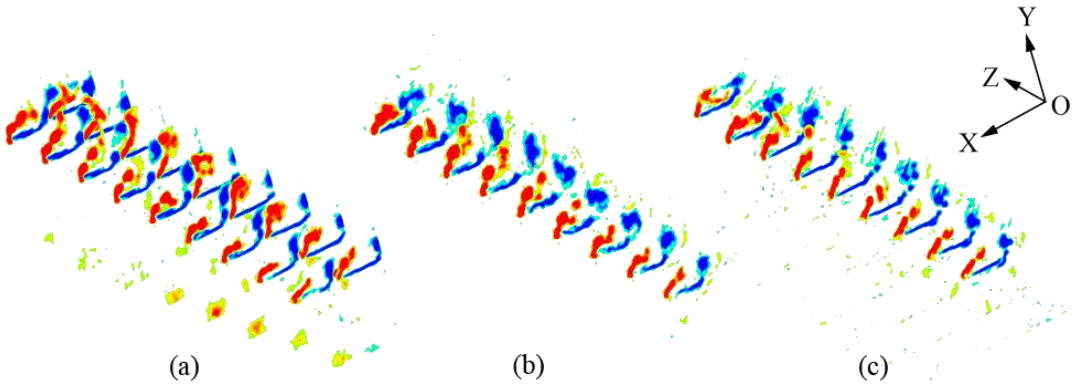


Fig. 14. Comparison of three-dimensional vorticity at the mid-downstroke of the forewing: (a) in-phase flapping; (b) isolated forewing flapping; (c) isolated hindwing flapping.

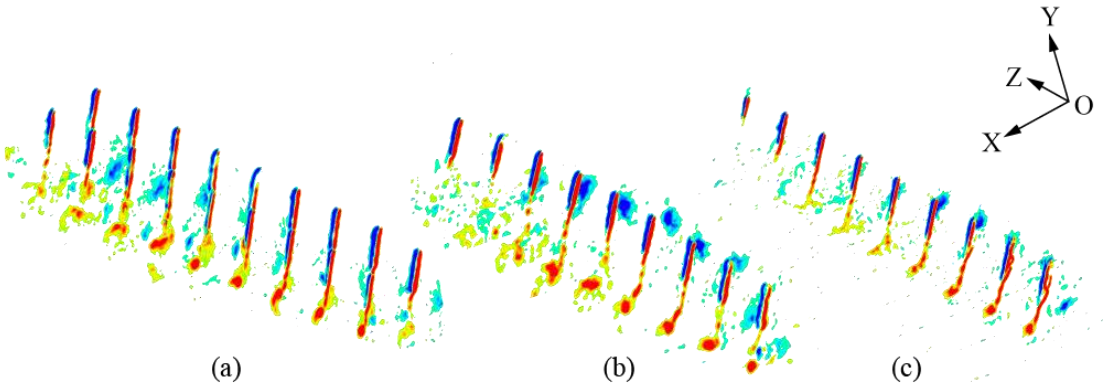


Fig. 15. Comparison of three-dimensional vorticity at the mid-upstroke of the forewing: (a) in-phase flapping; (b) isolated forewing flapping; (c) isolated hindwing flapping.

Fig. 16(a) shows the three-dimensional flow field of out-of-phase flapping when the forewing is at the mid-downstroke. Fig. 16(b,c) shows the three-dimensional flow fields of the isolated forewing and isolated hindwing at the same instant, respectively. At this instant, the forewing is at the mid-downstroke, while the hindwing is at the mid-upstroke. By comparing the three-dimensional flow fields of out-of-phase flapping and isolated-wing flapping, it can be seen that, under the induced-flow effect, the leading-edge vortex of the hindwing detaches from the wing surface and moves toward the trailing-edge vortex of the forewing. This flow characteristic is consistent with the two-dimensional analysis of the inter-wing flow field during the mid-downstroke of the forewing under out-of-phase flapping in Section 3.2.2.

Fig. 17(a) shows the three-dimensional flow field of out-of-phase flapping when the forewing is at the mid-upstroke. Fig. 17(b,c) shows the three-dimensional flow fields of the isolated forewing and isolated hindwing at the same instant, respectively. At this instant, the forewing is at the mid-upstroke, while the hindwing is at the mid-downstroke. By comparing the three-dimensional flow fields of out-of-phase flapping and isolated-wing flapping, it can be seen that, under the induced-flow effect, the size of the leading-edge vortex of the hindwing decreases. This reduction in the apparent LEV size is consistent with the local induced-flow modification observed in Fig. 13, suggesting that the forewing–hindwing interaction affects both the downward flow and the vortex structures around the hindwing during its downstroke.

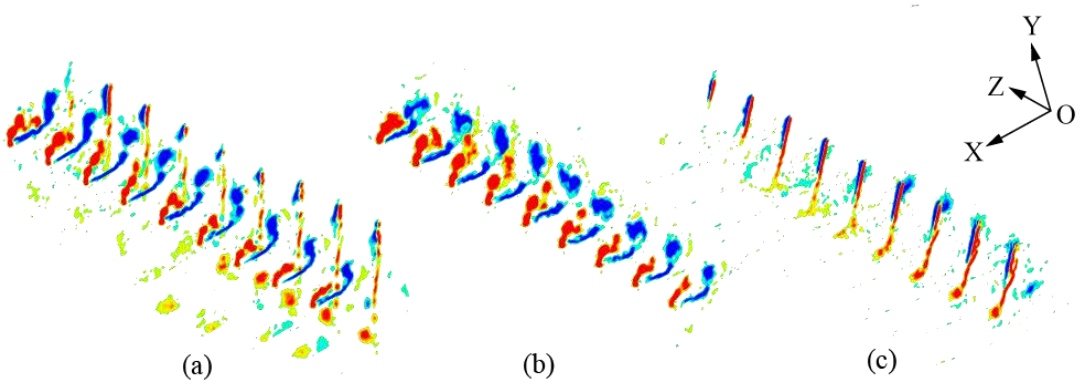


Fig. 16. Comparison of three-dimensional vorticity at the mid-downstroke of the forewing: (a) out-of-phase flapping; (b) isolated forewing flapping; (c) isolated hindwing flapping.

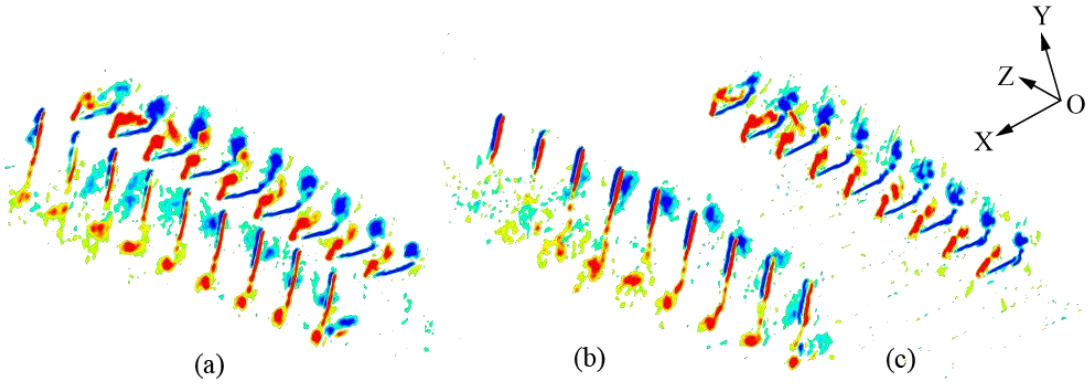


Fig. 17. Comparison of three-dimensional vorticity at the mid-upstroke of the forewing: (a) out-of-phase flapping; (b) isolated forewing flapping; (c) isolated hindwing flapping.

3.3 Induced-Flow Mechanism for Lift Differences between In-Phase and Out-of-Phase Flapping

Based on the analyses in Fig. 10-Fig. 13, the flow fields at the characteristic instants T = 0.25 and T = 0.75 under λ = 0° and λ = 180° show that inter-wing

aerodynamic interaction mainly results from the influence of induced flow generated during the relative motion of the forewing and hindwing. The effect of inter-wing interaction on lift differs under different phase differences. Under in-phase flapping, the wings move in the same direction and generate induced flow that is favorable for lift enhancement, thereby increasing the mean lift of both the forewing and hindwing. Under out-of-phase flapping, the wings move in opposite directions and generate induced flow that is unfavorable for lift enhancement, thereby reducing the mean lift of both wings. This inter-wing interaction between the forewing and hindwing is summarized as the induced-flow effect. That is, when the forewing and hindwing interact during motion, the flapping motion of one wing induces changes in the flow field around the other wing, which ultimately affects aerodynamic force generation. The aerodynamic influence of the induced-flow effect under in-phase and out-of-phase flapping is further illustrated by the following schematics. Fig. 18(a) shows the schematic flow field of the isolated forewing at the mid-downstroke. During the downstroke of an isolated wing, a leading-edge vortex and a trailing-edge vortex are generated at the leading and trailing edges, respectively. Under the action of this vortex pair, a downwash flow is formed. Fig. 18(b) shows the schematic flow field of tandem wings under in-phase flapping at the same instant. At this instant, both the forewing and hindwing are at the mid-downstroke. Since the two wings are close to each other and move downward synchronously, they drive the flow that originally forms the forewing trailing-edge vortex and the hindwing leading-edge vortex to move downward, as shown by the red streamlines in Fig. 18(b). As a result, the flow rate of the downwash increases, which is beneficial to lift enhancement.

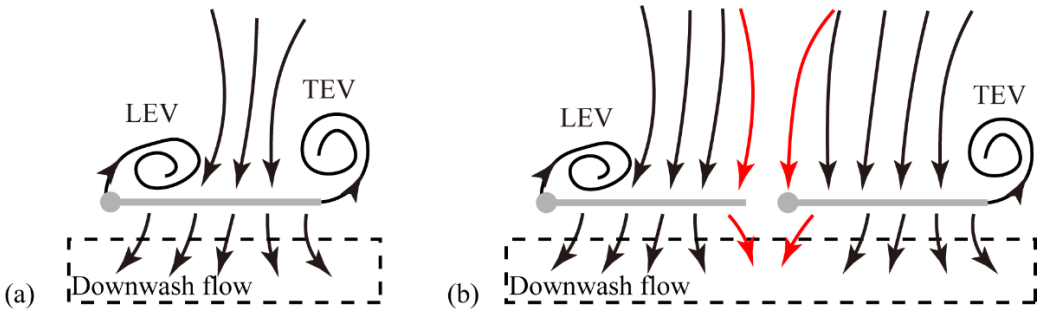


Fig. 18. Schematic interpretation of the induced-flow interaction during in-phase flapping at T = 0.25, based on the PIV observations in Fig. 10 and Fig. 14: (a) isolated-wing flapping; (b) in-phase flapping.

Fig. 19(a) shows the schematic flow field of the isolated forewing at the mid-upstroke. During the upstroke of an isolated wing, the surrounding flow is deflected upward. Fig. 19(b) shows the schematic flow field of tandem wings under out-of-phase flapping at the same instant. At this instant, the forewing is at the mid-upstroke, while the hindwing is at the mid-downstroke. The flow deflection caused by the upstroke of the forewing, as shown by the green streamlines in Fig. 19(b), affects the downwash generated by the hindwing during the downstroke. As a result, the velocity of the downwash decreases, which is unfavorable for lift generation.

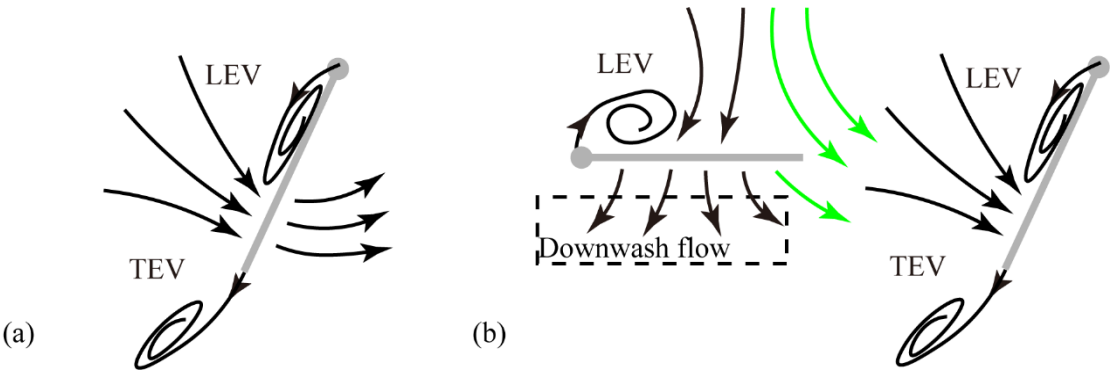


Fig. 19. Schematic interpretation of the induced-flow interaction during out-of-phase flapping at T = 0.75, based on the PIV observations in Fig. 13 and Fig. 17: (a) isolated-wing flapping; (b) out-of-phase flapping.

Therefore, under the induced-flow effect, in-phase flapping generates a larger mean lift, whereas out-of-phase flapping generates a smaller mean lift. This is consistent with the experimental force results in Section 3.2.1, where the force characteristics under in-phase and out-of-phase flapping were analyzed. The induced-flow effect can also be applied to the flapping strategy design of tandem-wing MAVs. During in-phase flapping, the distance between the forewing and hindwing should be reduced as much as possible. This allows the induced flow generated by the same-direction motion of the wings to be used for lift enhancement. In contrast, during out-of-phase flapping, the distance between the forewing and hindwing should be increased as much as possible. This can reduce the negative influence of opposite-direction wing motion on lift generation.

4. Discussion and Conclusions

This study combined force measurements and phase-resolved PIV measurements to investigate inter-wing aerodynamic interaction in dragonfly-like tandem flapping wings. The main conclusions are as follows:

(1) To address missing and distorted flow-field information caused by optical blockage from the non-target wing and reflection and refraction at the wing surfaces during tandem-wing PIV measurements, this study employed force-guided selection of characteristic cases, phase-resolved alignment based on the target wing, and phase-locked measurements of separate flow-field regions. These measures reduced optical interference and enabled the acquisition of inter-wing flow-field information under representative conditions. The experimentally observed changes in local induced flow and vortex structures provide complementary experimental evidence for the inter-wing interactions described in previous numerical studies.

(2) The forewing–hindwing phase difference affects lift generation by modifying inter-wing induced flow and vortex structures. During the mid-downstroke of in-phase flapping, the same-direction motion of the two wings enhances the downward induced flow between them and modifies the forewing trailing-edge vortex and hindwing leading-edge vortex, creating flow conditions favorable for lift enhancement. During out-of-phase flapping at 180°, the induced flow associated with the opposite-direction motion of the two wings weakens the local downwash of the

downstroking wing and is accompanied by detachment, displacement, or size reduction of the hindwing leading-edge vortex, adversely affecting lift generation. These flow-field characteristics provide a qualitative explanation for the force measurements, which show higher mean lift under in-phase flapping and the lowest mean lift under out-of-phase flapping at 180°.

The PIV measurements in this study focus on in-phase and out-of-phase flapping at 180°. Future measurements at additional phase differences, such as 30°, 90°, and 270°, could establish a more complete relationship among phase difference, vortex structures, and aerodynamic forces. In addition, the two-dimensional PIV section measurements and spanwise stitching used here cannot fully capture the transient three-dimensional flow during flapping. Future work could incorporate stereoscopic PIV, time-resolved PIV, or tomographic PIV to further resolve the three-dimensional velocity distribution and the spatiotemporal evolution of vortex structures. The effects of the water-tank walls on the measurements and the measurement errors introduced by experimental noise also require further quantitative assessment to strengthen the evaluation of measurement reliability and uncertainty.

Author contributions

Conceptualization, S.G., M.Z., G.S., J.L. and Q.L.; Methodology, S.G., M.Z., G.S. and J.L.; Software, S.G.; Validation, S.G., M.Z., G.S. and J.L.; Formal analysis, S.G.; Investigation, S.G., M.Z., G.S. and J.L.; Resources, M.Z., G.S., J.L. and Q.L.; Data curation, S.G.; Writing—original draft preparation, S.G.; Writing—review and editing, S.G., M.Z., G.S., J.L. and Q.L.; Visualization, S.G., M.Z., G.S. and J.L.; Supervision, J.L. and Q.L.; Project administration, J.L. and Q.L.; Funding acquisition, M.Z. and G.S. All authors have read and agreed to the published version of the manuscript.

Acknowledgment

This research was funded by National Natural Science Foundation of China (Nos. U2441278 and U24A20141), National Science and Technology Major Project (No. 2017-II-0005-0018-JX), Sichuan Science and Technology Program (No. 2025ZYD0188), the Fundamental Research Funds for the Central Universities of China. In addition, the authors would like to thank Liansong Peng for his support and assistance during the course of this study.

Data availability

The data that support the findings of this study are available from the corresponding authors upon reasonable request.

Competing interests

The authors declare no competing interests.

References

Adrian RJ (1991) Particle-Imaging Techniques for Experimental Fluid Mechanics. Annu Rev Fluid Mech 23:261–304.

https://doi.org/10.1146/annurev.fl.23.010191.001401

Alexander DE (1984) Unusual Phase Relationships Between The Forewings And Hindwings In Flying Dragonflies. J Exp Biol 109:379–383. https://doi.org/10.1242/jeb.109.1.379

Azuma A, Watanabe T (1988) Flight Performance of a Dragonfly. J Exp Biol 137:221–252. https://doi.org/10.1242/jeb.137.1.221

Berman GJ, Wang ZJ (2007) Energy-minimizing kinematics in hovering insect flight. J Fluid Mech 582:153–168. https://doi.org/10.1017/S0022112007006209

Birch JM, Dickinson MH (2003) The influence of wing–wake interactions on the production of aerodynamic forces in flapping flight. J Exp Biol 206:2257–2272. https://doi.org/10.1242/jeb.00381

Bomphrey RJ, Godoy-Diana R (2018) Insect and insect-inspired aerodynamics: unsteadiness, structural mechanics and flight control. Curr Opin Insect Sci 30:26–32. https://doi.org/10.1016/j.cois.2018.08.003

Broering TM, Lian Y, Henshaw W (2012) Numerical Investigation of Energy Extraction in a Tandem Flapping Wing Configuration. AIAA J 50:2295–2307. https://doi.org/10.2514/1.J051104

Broering TM, Lian Y-S (2012) The effect of phase angle and wing spacing on tandem flapping wings. Acta Mech Sin 28:1557–1571. https://doi.org/10.1007/s10409-012-0210-8

Chin DD, Lentink D (2016) Flapping wing aerodynamics: from insects to vertebrates. J Exp Biol 219:920–932. https://doi.org/10.1242/jeb.042317

Dickinson MH, Lehmann F-O, Sane SP (1999) Wing Rotation and the Aerodynamic Basis of Insect Flight. Science 284:1954–1960. https://doi.org/10.1126/science.284.5422.1954

Ellington CP, Van Den Berg C, Willmott AP, Thomas ALR (1996) Leading-edge vortices in insect flight. Nature 384:626–630. https://doi.org/10.1038/384626a0

Floreano D, Wood RJ (2015) Science, technology and the future of small autonomous drones. Nature 521:460–466. https://doi.org/10.1038/nature14542

Lan S, Mao S (2001) Aerodynamic force and flow structures of two airfoils in flapping motions. Acta Mech Sin 17:310–331. https://doi.org/10.1007/BF02487459

Lentink D, Dickinson MH (2009) Rotational accelerations stabilize leading edge vortices on revolving fly wings. J Exp Biol 212:2705–2719. https://doi.org/10.1242/jeb.022269

Li C, Dong H (2017) Wing kinematics measurement and aerodynamics of a dragonfly in turning flight. Bioinspir Biomim 12:026001. https://doi.org/10.1088/1748-3190/aa5761

Liang J, Zheng M, Pan T, et al (2025) Development of a Dragonfly-Inspired High Aerodynamic Force Flapping-Wing Mechanism Using Asymmetric Wing Flapping Motion. Biomimetics 10:309. https://doi.org/10.3390/biomimetics10050309

Maybury WJ, Lehmann F-O (2004) The fluid dynamics of flight control by kinematic phase lag variation between two robotic insect wings. J Exp Biol 207:4707–4726. https://doi.org/10.1242/jeb.01319

Nabawy MRA (2023) A simple model of wake capture aerodynamics. J R Soc

Interface 20:20230282. https://doi.org/10.1098/rsif.2023.0282

Nakata T, Henningsson P, Lin H-T, Bomphrey RJ (2020) Recent progress on the flight of dragonflies and damselflies. Int J Odonatol 23:41–49. https://doi.org/10.1080/13887890.2019.1688502

Peng L, Zheng M, Pan T, et al (2021) Tandem-wing interactions on aerodynamic performance inspired by dragonfly hovering. R Soc Open Sci 8:202275. https://doi.org/10.1098/rsos.202275

Raffel M, Willert CE, Scarano F, et al (2018) Particle Image Velocimetry: A Practical Guide. Springer International Publishing, Cham

Rüppell G, Hilfert-Rüppell D (2020) Rapid acceleration in Odonata flight: highly inclined and in-phase wing beating. Int J Odonatol 23:63–78. https://doi.org/10.1080/13887890.2019.1688017

Salami E, Montazer E, Ward TA, et al (2022) Aerodynamic Performance of a Dragonfly-Inspired Tandem Wing System for a Biomimetic Micro Air Vehicle. Front Bioeng Biotechnol 10:787220. https://doi.org/10.3389/fbioe.2022.787220

Song F, Yan Y, Sun J (2023) Review of insect-inspired wing micro air vehicle. Arthropod Struct Dev 72:101225. https://doi.org/10.1016/j.asd.2022.101225

Sun M, Lan SL (2004) A computational study of the aerodynamic forces and power requirements of dragonfly (*Aeschna juncea*) hovering. J Exp Biol 207:1887–1901. https://doi.org/10.1242/jeb.00969

Takahashi H, Concordel A, Paik J, Shimoyama I (2016) The Effect of the Phase Angle between the Forewing and Hindwing on the Aerodynamic Performance of a Dragonfly-Type Ornithopter. Aerospace 3:4. https://doi.org/10.3390/aerospace3010004

Usherwood JR, Lehmann F-O (2008) Phasing of dragonfly wings can improve aerodynamic efficiency by removing swirl. J R Soc Interface 5:1303–1307. https://doi.org/10.1098/rsif.2008.0124

Wakeling JM, Ellington CP (1997a) Dragonfly Flight : II. Velocities, Accelerations and Kinematics of Flapping Flight. J Exp Biol 200:557–582. https://doi.org/10.1242/jeb.200.3.557

Wakeling JM, Ellington CP (1997b) Dragonfly Flight: I. Gliding Flight and Steady-State Aerodynamic Forces. J Exp Biol 200:543–556. https://doi.org/10.1242/jeb.200.3.543

Wang JK, Sun M (2005) A computational study of the aerodynamics and forewing-hindwing interaction of a model dragonfly in forward flight. J Exp Biol 208:3785–3804. https://doi.org/10.1242/jeb.01852

Wang ZJ, Russell D (2007) Effect of Forewing and Hindwing Interactions on Aerodynamic Forces and Power in Hovering Dragonfly Flight. Phys Rev Lett 99:148101. https://doi.org/10.1103/PhysRevLett.99.148101

Westerweel J (1997) Fundamentals of digital particle image velocimetry. Meas Sci Technol 8:1379–1392. https://doi.org/10.1088/0957-0233/8/12/002

Yang X, Wang H, Luo Y, et al (2025) Coupled Effects of Spatial Configuration and Phase Difference on the Aerodynamics of Dragonfly-Inspired Tandem Wings

Zheng M, Deng Y, Liang J, et al (2026) Unsteady aerodynamic mechanisms of

wing flexibility in dragonfly flapping flight. J Fluids Struct 140:104471. https://doi.org/10.1016/j.jfluidstructs.2025.104471

Zheng M, Peng L, Su G, et al (2024) Experimental Investigation on Aerodynamic Performance of Inclined Hovering with Asymmetric Wing Rotation. Biomimetics 9:225. https://doi.org/10.3390/biomimetics9040225

Zheng Y, Wu Y, Tang H (2016) An experimental study on the forewing–hindwing interactions in hovering and forward flights. Int J Heat Fluid Flow 59:62–73. https://doi.org/10.1016/j.ijheatfluidflow.2015.12.006